Model-Based Estimation of 3-D Stiffness Parameters in Photonic-Force Microscopy

P. Thévenaz*, A. S. G. Singh, E. Bertseva, J. Lekki, A. J. Kulik, and M. Unser

***Abstract*—We propose a system to characterize the 3-D diffusion properties of the probing bead trapped by a photonic-force microscope. We follow a model-based approach, where the model of the dynamics of the bead is given by the Langevin equation. Our procedure combines software and analog hardware to measure the corresponding stiffness matrix. We are able to estimate all its elements in real time, including off-diagonal terms. To achieve our goal, we have built a simple analog computer that performs a continuous preprocessing of the data, which can be subsequently digitized at a much lower rate than is otherwise required. We also provide an effective numerical algorithm for compensating the correlation bias introduced by a quadrant photodiode detector in the microscope. We validate our approach using simulated data and show that our bias-compensation scheme effectively improves the accuracy of the system. Moreover, we perform experiments with the real system and demonstrate real-time capabilities. Finally, we suggest a simple adjunction that would allow one to determine the mass matrix as well.**

***Index Terms*—Brownian motion, Langevin process, quadrant photodiode (QPD).**

I. Introduction

A PHOTONIC-FORCE microscope (PFM) is an instrument that uses a focused laser beam to loosely trap a micrometer-sized bead within some liquid medium. Random thermal fluctuations act upon molecules of the medium, which collide with the bead, setting it into motion, while the focused laser pulls it back to a resting position. Using optical means, the whereabouts of the bead is recorded through time.

The appropriate statistical analysis of the recorded path provides insights on the properties of the medium at the location of the bead [1]–[6]. Not only do thermally induced fluctuations of the position of the trapped bead provide access to the viscoelastic properties of aqueous environments [1], they also provide a valuable tool to measure the mechanical properties of single motor molecules with high resolution [7]. Moreover, a PFM can be used to image in 3-D the topology of a polymer network [8]. Unfortunately, these analyses require the processing of a high amount of data. Until now, the calculations have been done offline, which is extremely time-demanding.

In this paper, we provide the detailed explanations of a system that we first proposed in [9], where we had added to the traditional PFM a combination of software and analog hardware. When used jointly, these additional components allow for the real-time estimation of the stiffness matrix of the trap, including of its off-diagonal elements. In addition, we propose another modification that will allow for the determination of the mass matrix of the bead, also in real time and in 3-D.

The roadmap for this paper is as follows: In Section II, we introduce and justify the use of the Langevin equation to model the dynamics of the probe used in PFM. We also adopt a signal-processing formalism to simplify the analysis and resolution of the corresponding stochastic differential equation. The main contribution is then to be found in Sections III and IV, where we explain how we harness the raw data. We present experiments in Section V, before we conclude in Section VI.

II. Langevin Process

A. Classical Analysis

We rely on Newtonian mechanics to describe the evolution of the position of a bead inside an optical trap, which balances four forces. The random driving force $(\sigma_0\, n)$ is assumed to be a scaled version of a centered Gaussian white noise n of unit variance. The scaling factor is σ_0. This force is imparted to the bead by its impact with molecules of the medium. Once set in motion, the bead experiences a viscous drag, which we model by a force that is proportional to the speed of the bead. (To keep this model simple, we ignore contributions, such as the hydrodynamic memory effect [10].) Once displaced, the bead is pulled back to its resting position x_0 by the optical trap. We model this as a spring that would exert a linear response over a range of about $\lambda_0/2$ in axial and $\lambda_0/4$ in lateral directions [11]. Moreover, we assume that the bead remains trapped at all times

Manuscript received October 1, 2009; revised January 20, 2010. Date of publication March 8, 2010; date of current version June 3, 2010. This work was funded by GEBERT-RÜF STIFTUNG under Project GRS-012/06. *Asterisk indicates corresponding author.*

*P. Thévenaz is with the École polytechnique fédérale de Lausanne (EPFL), EPFL/School of Engineering (STI)/Institut de microtechnique (IMT)/Laboratoire d'imagerie biomédicale (LIB), CH–1015 Lausanne VD, Switzerland (e-mail: philippe.thevenaz@epfl.ch).

A. S. G. Singh and M. Unser are with the École polytechnique fédérale de Lausanne (EPFL), EPFL/School of Engineering (STI)/Institut de microtechnique (IMT)/Laboratoire d'imagerie biomédicale (LIB), CH–1015 Lausanne VD, Switzerland (e-mail: amardeep.singh@meduniwien.ac.at; michael.unser@epfl.ch).

E. Bertseva is with the École polytechnique fédérale de Lausanne (EPFL), EPFL/School of Basic Sciences (SB)/Institut de physique de la matière complexe (IPMC)/Laboratoire de nanostructures et nouveaux matériaux electroniques (LNNME), CH–1015 Lausanne VD, Switzerland (e-mail: elena.bertseva@epfl.ch).

J. Lekki is with the Institute of Nuclear Physics, Polish Academy of Sciences, 31-342 Krakow, Poland (e-mail: janusz.lekki@ifj.edu.pl).

A. J. Kulik is with the École polytechnique fédérale de Lausanne (EPFL), EPFL/School of Basic Sciences (SB)/Institut de physique des systèmes biologiques (IPSB)/Laboratoire de physique de la matière vivante (LPMV), Bât. sciences physiques UNIL, CH–1015 Lausanne VD, Switzerland (e-mail: andrzej.kulik@epfl.ch).

Color versions of one or more of the figures in this paper are available online at http://ieeexplore.ieee.org.

Digital Object Identifier 10.1109/TNB.2010.2043260

1536-1241/$26.00 © 2010 IEEE

Authorized licensed use limited to: EPFL LAUSANNE. Downloaded on June 10,2010 at 13:35:30 UTC from IEEE Xplore. Restrictions apply.

and never wanders beyond this linear range. Finally, the inertia of the bead provides the reaction force. In 1-D, we therefore express the dynamics of the system by

$$m\,\ddot{x} + \gamma\,\dot{x} + \kappa\,(x - x_0) = \sigma_0\,n \tag{1}$$

which is called the Langevin equation. Here, m is the mass of the bead, γ is the coefficient of drag, κ is the spring stiffness, and x is the position of the bead. The value $\sigma_0 = \sqrt{2\,k_\mathrm{B}\,T}$ is given by the Sutherland–Einstein–Smoluchowski relation, where T is the temperature of the medium surrounding the bead and k_B is the Boltzmann constant. We consider that m, γ, and κ depend neither on time nor on space, at least locally. However, their large-scale evolution, particularly over space, is what we are interested in.

To make the system tractable, further assumptions are required [12]. Among them, the system is assumed to be memoryless and to satisfy the fluctuation–dissipation relations. Then, (1) can be extended to 3-D [13]. This leads to

$$\mathbf{M}\,\ddot{\mathbf{x}} + \mathbf{\Gamma}\,\dot{\mathbf{x}} + \mathbf{K}\,(\mathbf{x} - \mathbf{x}_0) = \mathbf{F}\,\mathbf{n} \tag{2}$$

where $\mathbf{M}$ is the mass matrix of the bead, $\mathbf{\Gamma}$ is a friction matrix related to the medium, $\mathbf{K}$ is the stiffness matrix of the optical trap, $\mathbf{x}_0$ is the resting position of the bead, and where the product of the matrix $\mathbf{F}$ with the noise vector $\mathbf{n} = (n_1, n_2, n_3)$ represents the contribution of the driving force. Componentwise, $n_i \in \mathcal{N}(0,1)$ is again a centered, unit-variance, Gaussian, white noise, while $\mathbf{F}$ depends on $\mathbf{\Gamma}$ and on the temperature. In all generality, this system has no less than 31 free parameters (the temperature, the three coordinates of $\mathbf{x}_0$, along with the elements of the three (3×3) matrices $\mathbf{M}$, $\mathbf{\Gamma}$, and $\mathbf{K}$). As our goal is to fit the parameters of the Langevin model to the experimental path taken by the bead, we simplify (2) by assuming that all matrices are symmetric. Nonetheless, we retain off-diagonal terms, which is one important contribution of our method. Under these conditions, a classical result from [12] is that the random position $\mathbf{x}$ that satisfies (2) has an expected value $\mathrm{E}\{\mathbf{x}\} = \mathbf{x}_0$, which does not depend on time. Moreover, $\mathbf{x}$ follows a Gaussian distribution given by

$$p(\mathbf{x}) = \frac{1}{\sqrt{(2\,\pi)^3\;|\det(\mathbf{C})|}}\,\mathrm{e}^{-1/2\,(\mathbf{x}-\mathbf{x}_0)^\mathsf{T}\,\mathbf{C}^{-1}\,(\mathbf{x}-\mathbf{x}_0)} \tag{3}$$

where the autocovariance of the bead displacement is found to be

$$\mathbf{C} = k_\mathrm{B}\,T\,\mathbf{K}^{-1}. \tag{4}$$

B. Signal-Processing Perspective

In this section, we undertake the analysis of the 1-D Langevin equation with concepts and notations familiar to a signal-processing audience. In particular, we rederive a result concerning the variance of the position x in (1). While the result itself is well-known, the use of signal-processing tools makes the self-contained derivation particularly simple and accessible.

An operator G takes a function as argument and transforms it into another function. A *convolutional* operator is such that it is fully characterized by its impulse response $\mathrm{G}\{\delta\}$, where δ is the Dirac distribution. For instance, D^n is the operator that converts a functional argument x into its nth derivative $x^{(n)}$, in particular, $\mathrm{D}^0 = \mathrm{I}$ is the identity. We observe that D^n is convolutional, with impulse response $\delta^{(n)}$.

In (1), we take the view that $(\sigma_0\,n)$ can be obtained by applying a convolutional operator G to the signal x. Without loss of generality, we can assume $x_0 = 0$, which leads to

$$\begin{aligned}\mathrm{G}\{x\} &= m\,\mathrm{D}^2\{x\} + \gamma\,\mathrm{D}\{x\} + \kappa\,\mathrm{I}\{x\}\\ &= m\,\left((\mathrm{D} - s_1\,\mathrm{I})\,(\mathrm{D} - s_2\,\mathrm{I})\right)\{x\}\end{aligned}$$

where we have that

$$s_1 = \frac{1}{2\,m}\left(-\gamma + \sqrt{\gamma^2 - 4\,\kappa\,m}\right)$$

and

$$s_2 = \frac{1}{2\,m}\left(-\gamma - \sqrt{\gamma^2 - 4\,\kappa\,m}\right).$$

Next, we want to find ρ, such that $\mathrm{G}\{\rho\} = \delta$. The function ρ is called the Green function of the operator, it is defined up to an additive component ρ_0 that belongs to the null-space of G, with $\mathrm{G}\{\rho_0\}(t) = 0\ \forall t \in \mathbb{R}$. (We choose to ignore ρ_0 because this component is associated with the boundary conditions of the system, while we are interested only in its steady-state regime.) Using $\mathcal{F}$ to indicate the Fourier transform, with the pulsation $\omega \in \mathbb{R}$, we have that

$$\begin{aligned}\mathcal{F}\{\rho\}(\omega) &= \frac{1}{\mathcal{F}\{\mathrm{G}\{\delta\}\}(\omega)}\\ &= \frac{1}{m\,(\mathrm{j}\,\omega - s_1)\,(\mathrm{j}\,\omega - s_2)}\\ &= \hat{\rho}(\omega)\end{aligned} \tag{5}$$

where we have taken advantage of the Fourier property that maps convolutions in the time domain to multiplications in the pulsation domain. There, j is the imaginary unit, while the forward Fourier transform $\hat{f}$ of a function f is defined as $\hat{f}(\omega) = \int_\mathbb{R} f(t)\,\mathrm{e}^{-\mathrm{j}\,\omega\,t}\,\mathrm{d}t$. (In the case of the forward Fourier transform, the signal-processing conventions involve the absence of a $(2\,\pi)$ factor and the presence of a negative sign in the exponential.) Since $\Re(s_1) < 0$ and $\Re(s_2) < 0$, the solution is well-defined and we have that

$$\forall t \in \mathbb{R} : \rho(t) = \frac{1}{m}\left((u(\cdot)\,\mathrm{e}^{s_1\,\cdot}) * (u(\cdot)\,\mathrm{e}^{s_2\,\cdot})\right)(t),$$

where u is the unit-step function with $\mathrm{D}\{u\} = \delta$, and where the operation '$*$' is used to indicate the convolution of the two signals x and y, defined as $(x * y)\,(t) = \int_\mathbb{R} x(\tau)\,y(t-\tau)\,\mathrm{d}\tau$.

From $\mathrm{G}\{\rho\} = \delta \Rightarrow \mathrm{G}\{\sigma_0\,\rho * n\} = \sigma_0\,\delta * n = \sigma_0\,n = \mathrm{G}\{x\}$, we infer that the solution of the Langevin equation is as follows:

$$x = \sigma_0\,\rho * n. \tag{6}$$

This last equation suggests that the position of the bead can be obtained by filtering the driving force acting upon it, which provides a convenient way to synthesize trajectories when we validate our approach, in Section V-A. Thus, the power spectral

Authorized licensed use limited to: EPFL LAUSANNE. Downloaded on June 10,2010 at 13:35:30 UTC from IEEE Xplore. Restrictions apply.

density of the position is $\mathrm{S}\{x\} = \sigma_0^2\ |\hat{\rho}|^2$, where the power spectral density of $(\sigma_0\, n)$ is $\sigma_0^2 = 2\, k_\mathrm{B}\, T\, \gamma$. Taking advantage of (5), and taking an inverse Fourier transform $\mathrm{R}\{x\} = \mathcal{F}^{-1}\{\mathrm{S}\{x\}\}$, we can obtain the explicit form of the autocorrelation of x in terms of a lag $\tau \in \mathbb{R}$ as follows:

$$\mathrm{R}\{x\}(\tau) = \frac{k_\mathrm{B}\, T}{\kappa}\, \mathrm{e}^{-(\gamma/2\,m)\,|\tau|}\, \left(\cos(\Omega\,\tau) + \frac{\gamma}{2\,\Omega\,m}\, \sin(\Omega\ |\tau|)\right)$$

with

$$\Omega = \sqrt{\frac{\kappa}{m} - \left(\frac{\gamma}{2\,m}\right)^2}.$$

Finally, the variance of x is given by $\mathrm{R}\{x\}(0)$, so that $\mathrm{VAR}\{x\} = k_\mathrm{B}\, T/\kappa$. Thus, the spring term $\kappa \neq 0$ is responsible for destroying the Brownian quality of the process, which would otherwise be characterized by an unbounded variance. This result generalizes to the 3-D Langevin process (2) as well.

III. Proposed System

The overall strategy that we pursue here is first to obtain an estimate of the autocovariance of the bead displacement, and then, to get the stiffness matrix of the optical trap through (4). We propose to obtain the autocovariance by using an analog computer. This has two main benefits: 1) we can spare the high-speed sampling, recording, and especially, processing of the huge number of individual samples of the trajectory of the bead that would otherwise be required by an offline approach; 2) in our online approach, all the data continuously contribute to the final measurements, while in an offline approach, whatever happens to the signal is lost, except at the precise instants when it is sampled. (While an optimal procedure to fill these gaps exists [14], [15], this procedure is not trivial.)

We defer the description of our analog computer until Section IV-A, because before any data are processed, either in analog or digital fashion, we have to remember that the 3-D displacement of the bead is measured at the output of an ultrafast quadrant photodiode (QPD) that collects interference patterns [16]. Thus, the characteristics of the QPD are going to play a significant role, which we detail in Section III-A.

A. Detector Response

The laser light that traps the bead also interferes with it. These interference patterns are collected by a QPD that measures the four intensities $\{Q_1, Q_2, Q_3, Q_4\}$, as schematized in Fig. 1. These quantities are not accessible directly, instead, the signal of the detector is returned as the triplet

$$\mathbf{y} = \begin{pmatrix} q_1\ ((Q_1 + Q_3) - (Q_2 + Q_4)) \\ q_2\ ((Q_1 + Q_2) - (Q_3 + Q_4)) \\ q_3\ (Q_1 + Q_2 + Q_3 + Q_4) \end{pmatrix} \tag{7}$$

where the set of coefficients $\{q_1, q_2, q_3\}$ translates the intensity Q, in lumen, into the measured signal $\mathbf{y}$, in volt. (Fortunately, the explicit knowledge of these coefficients is unnecessary.)

1) Traditional Model: To obtain the position of the bead for movements of small amplitude, it is customary to apply a simple linear conversion factor, so that $\tilde{x}_1 = y_1/\beta_1$, $\tilde{x}_2 = y_2/\beta_2$, and $\tilde{x}_3 = y_3/\beta_3$. The quantity $\tilde{\mathbf{x}}$, thus obtained is but an estimate of the true position $\mathbf{x}$ of the bead, which remains inaccessible. The coefficients $(\beta_1, \beta_2, \beta_3)$ result from a calibration procedure that involves the detection of a plateau in the spectrum of the measurements [17]. This simple procedure, however, assumes that the measurements are independent. In particular, it assumes that y_1 and y_2 do not themselves depend on y_3.

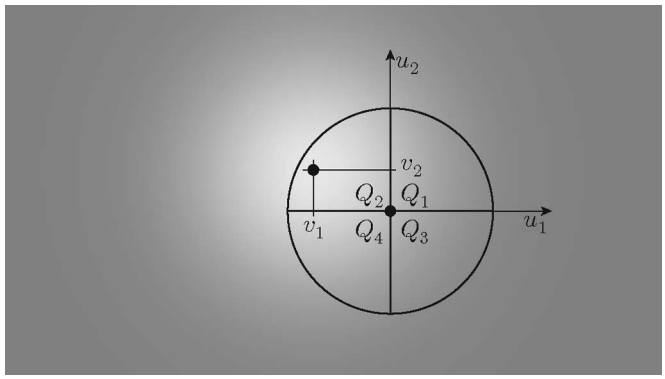

Fig. 1. Ultrafast QPD.

2) Refined Model: We now show that this independence is not consistent with even a very simple model of the QPD. We start by establishing a coordinate system that is centered on the junction of the quadrants and oriented in such a way that the coordinates are indicated by $\mathbf{u} = (u_1, u_2)$, as indicated in Fig. 1. Next, we make the hypothesis that the QPD has infinite extent, and that the interference pattern takes the form of a Gaussian beam centered on $\mathbf{v} = (v_1, v_2)$. Furthermore, we assume that the components of $\mathbf{v}$ are proportional to the lateral displacements of the bead with $v_1 \propto x_1$ and $v_2 \propto x_2$. Then, we choose to model the intensity reaching the QPD in each point by

$$q(\mathbf{u}) = Q_0\, \left(1 + \frac{x_3}{X_3}\right)\, \frac{1}{4\,\sigma_\mathrm{B}^2}\, \sqrt{2/\pi}\, \mathrm{e}^{-(\|\mathbf{u}-\mathbf{v}\|^2)/2\,\sigma_\mathrm{B}^2}$$

where Q_0 is a global illumination modulated by the axial position x_3 of the bead and X_3 is a quantity that models the degree of modulation. The width of the Gaussian beam is given by σ_B. The scaling factor $1/4\,\sigma_\mathrm{B}^2\, \sqrt{2/\pi}$ has been thrown in for notational convenience, to simplify the calculations that we are about to perform. This model of the detector does not do justice to any sort of diffraction patterns. Yet, it introduces a feature that we believe is crucial and shared by more refined models. On one hand, it encodes the lateral position (x_1, x_2) of the bead in the location (v_1, v_2) of the Gaussian spot on the QPD. On the other hand, the axial position is encoded by the intensity of the light, which is made to vary linearly (in a first-order approximation) with the axial position x_3 of the bead.

To obtain the intensity Q_i that reaches a quadrant of the photodiode, we then integrate q over the ith quadrant. Finally, we apply (7) to the outcome, which yields the measurement

$$\mathbf{y} = \begin{pmatrix} q_1\, Q_0\, \left(1 + \frac{x_3}{X_3}\right)\, \sqrt{\frac{\pi}{2}}\, \mathrm{erf}(\frac{v_1}{\sigma_\mathrm{B}\,\sqrt{2}}) \\ q_2\, Q_0\, \left(1 + \frac{x_3}{X_3}\right)\, \sqrt{\frac{\pi}{2}}\, \mathrm{erf}(\frac{v_2}{\sigma_\mathrm{B}\,\sqrt{2}}) \\ q_3\, Q_0\, \left(1 + \frac{x_3}{X_3}\right)\, \sqrt{\frac{\pi}{2}} \end{pmatrix}$$

Authorized licensed use limited to: EPFL LAUSANNE. Downloaded on June 10,2010 at 13:35:30 UTC from IEEE Xplore. Restrictions apply.

where the McLaurin expansion of the erf function is $\mathrm{erf}(z) = 2/\sqrt{\pi}\ \sum_{k\in\mathbb{N}}\ (-1)^k\ z^{2\,k+1}/\,(k!\ (2\,k+1))$. As can be seen, this expansion lacks second-order terms, which means that a linear approximation of erf is already good enough, at least for small arguments z. Applying this approximation, we obtain

$$\mathbf{y} = \begin{pmatrix} \frac{q_1\,Q_0}{\sigma_\mathrm{B}}\ v_1\ \frac{x_3+X_3}{X_3} \\ \frac{q_2\,Q_0}{\sigma_\mathrm{B}}\ v_2\ \frac{x_3+X_3}{X_3} \\ \frac{q_3\,Q_0}{X_3}\ \sqrt{\frac{\pi}{2}}\ (x_3+X_3) \end{pmatrix}.$$

We now make explicit the hypothesis that v_1 and v_2 are proportional to x_1 and x_2, respectively. To specify the appropriate constants of proportionality, we aggregate the unknown parameters q_i, Q_0, X_3, and σ_B, which leads to $(q_1\,Q_0/\sigma_\mathrm{B})\ v_1 = \beta_1\,x_1$, $(q_2\,Q_0/\sigma_\mathrm{B})\ v_2 = \beta_2\,x_2$, and $q_3\,Q_0/X_3\,\sqrt{\pi/2} = \beta_3$. This finally establishes that

$$\mathbf{y} = \begin{pmatrix} \beta_1\,x_1\ \frac{x_3+X_3}{X_3} \\ \beta_2\,x_2\ \frac{x_3+X_3}{X_3} \\ \beta_3\ (x_3+X_3) \end{pmatrix}. \tag{8}$$

Clearly, (8) contradicts the hypothesis of independence between the quantities y_1, y_2, and y_3 that was made in the traditional approach.

3) Alternative Model: To approach the issue of independence from another angle, we now forget about the Gaussian spot of Section III-A2. Turning the model on its heel, we make upfront the hypothesis that the light reaching a quadrant consists of three additive contributions, and a scaling factor. The first term is a baseline average illumination Q_0 that is shared by all quadrants. We let the second contribution be proportional to the position x_1; we choose to write the factor of proportionality as $\pm\beta_1/q_1$, with a positive sign for Q_1 and Q_3, and a negative sign otherwise, as suggested in Fig. 1. (For instance, we want to enforce that an increase of v_1 results in an increase of Q_1 and a similar decrease of Q_2.) The last additive contribution is proportional to the position x_2; the factor of proportionality is $\pm\beta_2/q_2$ with a positive sign for Q_1 and Q_2, and a negative sign otherwise. These intensity terms are responsible for encoding the lateral position of the bead. As earlier, we assume that they are modulated by its axial position and made to be proportional to $(x_3+X_3)/4\,X_3$, where X_3 is some constant offset. We write this *a priori* model as follows:

$$\begin{cases} Q_1 = \left(Q_0 + \frac{\beta_1}{q_1}\,x_1 + \frac{\beta_2}{q_2}\,x_2\right)\ \frac{x_3+X_3}{4\,X_3} \\ Q_2 = \left(Q_0 - \frac{\beta_1}{q_1}\,x_1 + \frac{\beta_2}{q_2}\,x_2\right)\ \frac{x_3+X_3}{4\,X_3} \\ Q_3 = \left(Q_0 + \frac{\beta_1}{q_1}\,x_1 - \frac{\beta_2}{q_2}\,x_2\right)\ \frac{x_3+X_3}{4\,X_3} \\ Q_4 = \left(Q_0 - \frac{\beta_1}{q_1}\,x_1 - \frac{\beta_2}{q_2}\,x_2\right)\ \frac{x_3+X_3}{4\,X_3}, \end{cases}$$

where $Q_0 = (\beta_3/q_3)\,X_3$ represents the total time-averaged illumination of the detector. Under the hypothesis that $X_3 \gg |x_3|$, this illumination is sufficiently large to ensure that reasonable changes in $\mathbf{x}$ lead to negative Q_i only with a vanishingly small probability, in the sense of (3).

Applying our alternative model to the system of measurements (7), we observe that the formal outcome is *again* given by (8), exactly. If we now set $Y_3 = \beta_3\,X_3$, then we can rewrite an equivalent version of (8) as follows:

$$\begin{cases} y_3 = \beta_3\,x_3 + Y_3 \\ y_1 = \beta_1\,x_1\,\frac{y_3}{Y_3} \\ y_2 = \beta_2\,x_2\,\frac{y_3}{Y_3}. \end{cases}$$

The major interest of this form is that every term is physically accessible: y_i is the voltage found at the ith output of the QPD, β_i is determined as in [17], and Y_3 is the temporal average of y_3 under the hypothesis that x_3 has the temporal average $\mathrm{E}\{x_3\} = 0$.

B. Temporal Average

The major consequence of either the model of Section III-A2 or Section III-A3 is the observation that the components of the measured signal are artificially coupled by the detector, which leads to a bias in its time-averaged value. Indeed, combining (4) and (8), we obtain the expected value of the measurements as follows:

$$\mathrm{E}\{\mathbf{y}\} = \begin{pmatrix} \frac{\beta_1}{X_3}\,k_\mathrm{B}\,T\,\left[\mathbf{K}^{-1}\right]_{13} \\ \frac{\beta_2}{X_3}\,k_\mathrm{B}\,T\,\left[\mathbf{K}^{-1}\right]_{23} \\ Y_3 \end{pmatrix} \tag{9}$$

under the hypotheses that prevail in the establishment of (3).

C. Autocovariance Matrix

Taking (8) and (9) into account, we can now express the autocovariance matrix of the measurements as follows:

$$\mathbf{\Sigma} = \mathrm{E}\{(\mathbf{y} - \mathrm{E}\{\mathbf{y}\})\ (\mathbf{y} - \mathrm{E}\{\mathbf{y}\})^\mathsf{T}\} \tag{10}$$

with matrix entries σ_{ij}. To do so explicitly, we need to calculate high-order moments. Fortunately, $\mathbf{x}$ is following the Gaussian distribution (3) for which explicit results are known [18]. This leads to

$$\begin{aligned} \sigma_{11} &= \beta_1^2\ \left(c_{11}\ \left(1 + \frac{1}{Y_3^2}\,\beta_3^2\,c_{33}\right) + \frac{1}{Y_3^2}\,\beta_3^2\,c_{13}^2\right) \\ \sigma_{12} &= \beta_1\,\beta_2\ \left(c_{12}\ \left(1 + \frac{1}{Y_3^2}\,\beta_3^2\,c_{33}\right) + \frac{1}{Y_3^2}\,\beta_3^2\,c_{13}\,c_{23}\right) \\ \sigma_{13} &= \beta_1\,\beta_3\,c_{13} \\ \sigma_{22} &= \beta_2^2\ \left(c_{22}\ \left(1 + \frac{1}{Y_3^2}\,\beta_3^2\,c_{33}\right) + \frac{1}{Y_3^2}\,\beta_3^2\,c_{23}^2\right) \\ \sigma_{23} &= \beta_2\,\beta_3\,c_{23} \\ \sigma_{33} &= \beta_3^2\,c_{33} \end{aligned} \tag{11}$$

where the terms c_{ij} are entries of the autocovariance matrix $\mathbf{C}$ of the displacements of the bead. In the sequel, we are going to establish a method to measure $\mathbf{\Sigma}$, so that we can invert (11) to compute $\mathbf{C}$, therefore, determining $\mathbf{K}$ by the way of (4).

IV. Analog Hardware Computations

A. Analog Hardware

While our system is fast enough to acquire the three components of $\mathbf{y}$ at a high sampling rate (typically, 1 MHz), we are

Authorized licensed use limited to: EPFL LAUSANNE. Downloaded on June 10,2010 at 13:35:30 UTC from IEEE Xplore. Restrictions apply.

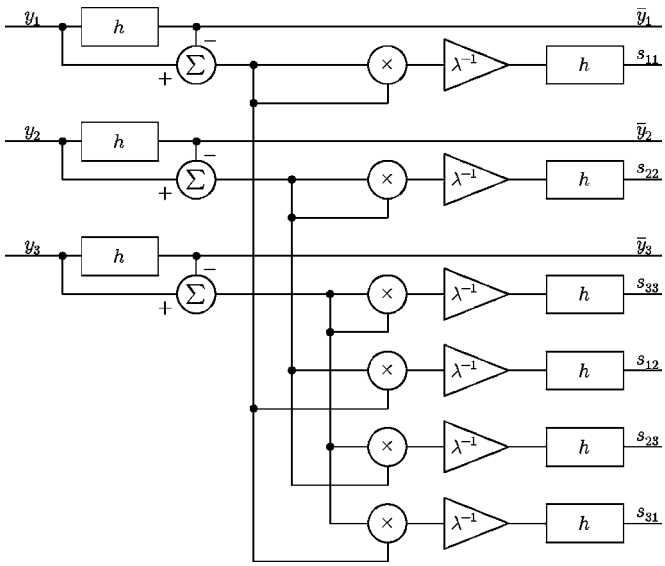

Fig. 2. Schematics of the analog processor used to get $\mathbf{S}$ given $\mathbf{y}$.

unable to perform their further processing in real time. Instead, we simply store them for later inspection. Because it would be difficult to obtain $\mathbf{K}^{-1}$ with online numeric computations, we have built an analog hardware device to provide us with an estimate of the the autocovariance $\mathbf{C}$ over a sliding time window.

Since $\mathbf{C} = \mathrm{E}\{(\mathbf{x} - \mathrm{E}\{\mathbf{x}\})\ (\mathbf{x} - \mathrm{E}\{\mathbf{x}\})^{\mathsf{T}}\}$, we need practical realizations of the expectation process E, which we obtain by virtue of an analog low-pass filter. Therefore, we get a time-varying access to the quantity $\mathrm{E}\{\mathbf{x}\}$ by creating the signal $\bar{\mathbf{y}}(t) = \int_{-\infty}^{t} \mathbf{y}(\tau)\, h(t-\tau)\, \mathrm{d}\tau$, where h is the impulse response of the filter. We have chosen to build h as the cascade of two standard first-order *RC* (active) filters, which ensures that h is causal and nonnegative, along with $\int_{-\infty}^{\infty} h(\tau)\, \mathrm{d}\tau = 1$. The latter condition ensures unbiasedness (see Appendix A), while the nonnegative condition ensures that the correlation matrix remains semipositive definite (see Appendix B), which is required for (3) to truly represent a Gaussian process. We have set the cutoff frequency of h to 500 Hz.

The signal $(y_i - \bar{y}_i)$ is then multiplied by $(y_j - \bar{y}_j)$. As this multiplication is realized in analog fashion, a scaling factor λ^{-1} is required to homogenize the physical units. In our case, this factor is such that multiplying together two signals of 1 V results in an output signal of 0.1 V, so that $\lambda = 10$. The outermost expectation operator defining $\mathbf{C}$ is finally implemented as yet another low-pass digital filter, with identical order, make, and cutoff frequency. This yields the components s_{ij} of the scatter matrix $\mathbf{S}$ that estimates the autocovariance matrix $\mathbf{\Sigma}$ of the measurements $\mathbf{y}$, up to the multiplicative factor λ. We give in Fig. 2, a schematic diagram of our device.

Because h is a low-pass filter, we can sample $s_{ij} \approx \sigma_{ij}/\lambda$ at a much lower rate (as low as 1 kHz in our current system) than we sample $\mathbf{y}$. In this way, we can now process the data numerically in real time. For instance, it becomes possible to reduce the influence of noise by computing a numeric time average of the slow signal.

B. Stiffness Matrix

Taking advantage of (11), it is possible to relate the inverse $\mathbf{K}^{-1}$ of the stiffness of the trap to the autocovariance matrix $\mathbf{S} \approx (1/\lambda)\, \mathbf{\Sigma}$ that we obtained with the aid of the hardware, we just described in Section IV-A. Fortunately, although (11) is quadratic in terms of c_{ij}, its inversion results in simple expressions. We have that

$$\begin{aligned}
\left[\mathbf{K}^{-1}\right]_{11} &= \frac{\lambda}{k_{\mathrm{B}}\, T} \left(\frac{s_{11}}{\beta_1^2} - \frac{\lambda}{Y_3^2}\, \frac{s_{13}^2}{\beta_1^2}\right) \left(1 + \frac{\lambda}{Y_3^2}\, s_{33}\right)^{-1} \\
\left[\mathbf{K}^{-1}\right]_{12} &= \frac{\lambda}{k_{\mathrm{B}}\, T} \left(\frac{s_{12}}{\beta_1\, \beta_2} - \frac{\lambda}{Y_3^2}\, \frac{s_{13}\, s_{23}}{\beta_1\, \beta_2}\right) \left(1 + \frac{\lambda}{Y_3^2}\, s_{33}\right)^{-1} \\
\left[\mathbf{K}^{-1}\right]_{13} &= \frac{\lambda}{k_{\mathrm{B}}\, T}\, \frac{s_{13}}{\beta_1\, \beta_3} \\
\left[\mathbf{K}^{-1}\right]_{22} &= \frac{\lambda}{k_{\mathrm{B}}\, T} \left(\frac{s_{22}}{\beta_2^2} - \frac{\lambda}{Y_3^2}\, \frac{s_{23}^2}{\beta_2^2}\right) \left(1 + \frac{\lambda}{Y_3^2}\, s_{33}\right)^{-1} \\
\left[\mathbf{K}^{-1}\right]_{23} &= \frac{\lambda}{k_{\mathrm{B}}\, T}\, \frac{s_{23}}{\beta_2\, \beta_3} \\
\left[\mathbf{K}^{-1}\right]_{33} &= \frac{\lambda}{k_{\mathrm{B}}\, T}\, \frac{s_{33}}{\beta_3^2}.
\end{aligned} \tag{12}$$

Alternatively, two components of this matrix can also be obtained from (9) as $\left[\mathbf{K}^{-1}\right]_{13} = (1/k_{\mathrm{B}}\, T)\, (\bar{y}_1\, \bar{y}_3)/(\beta_1\, \beta_3)$ and $\left[\mathbf{K}^{-1}\right]_{23} = (1/k_{\mathrm{B}}\, T)\, (\bar{y}_2\, \bar{y}_3)/(\beta_2\, \beta_3)$, where $(\bar{y}_1, \bar{y}_2, \bar{y}_3) \approx \mathrm{E}\{\mathbf{y}\}$. However, the analog-to-digital card we use to acquire the slow signal has eight entries only, while we would need nine to simultaneously access $\bar{\mathbf{y}}$ and $\mathbf{S}$. Therefore, we have relied on $\mathbf{S}$ alone while estimating $\mathbf{K}$.

To summarize, the method that we propose to obtain the stiffness of the optical trap results in a symmetric matrix $\mathbf{K}$ that takes cross-terms into account. It also compensates for the undesired correlations that the QPD detector creates between measurements. We have built an analog processor to handle the primary high-bandwidth signal. It generates a low-pass signal that we further process numerically. Our setup allows us to attain real-time performance. In Fig. 3, we provide a flowchart that summarizes the main ingredients of our approach.

C. Mass Matrix

The autocovariance matrix $\boldsymbol{\mathcal{C}}$ of the 6-D signal $(\mathbf{x}, \dot{\mathbf{x}})$ has been calculated in [12]. It is given by

$$\boldsymbol{\mathcal{C}} = \begin{pmatrix} k_{\mathrm{B}}\, T\, \mathbf{K}^{-1} & \mathbf{0} \\ \mathbf{0} & k_{\mathrm{B}}\, T\, \mathbf{M}^{-1} \end{pmatrix}$$

where we recognize the contribution of (4) of which we have already taken care. But the structure of $\boldsymbol{\mathcal{C}}$ also clearly suggests that a similar approach can be used to access the mass matrix $\mathbf{M}$, provided we start from the time derivative $\dot{\mathbf{y}}$ of the available signal $\mathbf{y}$. Fortunately, building an analog differentiator can be trivially achieved by an *RC* analog circuitry.

From (8), we write that

$$\dot{\mathbf{y}} = \begin{pmatrix} \beta_1\, \dot{x}_1 + \frac{\beta_1}{X_3}\, (\dot{x}_1\, x_3 + x_1\, \dot{x}_3) \\ \beta_2\, \dot{x}_2 + \frac{\beta_2}{X_3}\, (\dot{x}_2\, x_3 + x_2\, \dot{x}_3) \\ \beta_3\, \dot{x}_3 \end{pmatrix}.$$

Authorized licensed use limited to: EPFL LAUSANNE. Downloaded on June 10,2010 at 13:35:30 UTC from IEEE Xplore. Restrictions apply.

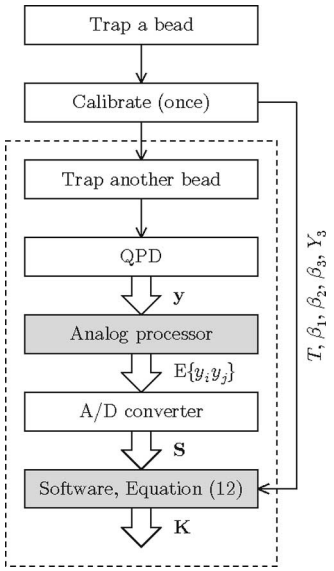

Fig. 3. Flowchart of our experimental setup. The QPD yields the analog signal $\mathbf{y}$, which is a vector with three components. This signal is transformed by our proposed analog processor into three autocovariances $\mathrm{E}\{y_i\, y_j\}$, $i = j$, and three cross-covariances $\mathrm{E}\{y_i\, y_j\}$, $i \neq j$. These get sampled and become the six independent components of the symmetric (3×3) covariance matrix $\mathbf{S}$. We then apply (12) to numerically compute the six independent components of the inverse of the symmetric (3×3) stiffness matrix $\mathbf{K}$. The grayed boxes indicate our specific contributions.

Because $\mathrm{E}\{\mathbf{x}\} = \mathbf{x}_0$ is not time-dependent, we have that $\mathrm{E}\{\dot{\mathbf{x}}\} = \mathbf{0}$. In addition, by examination of the off-diagonal block matrices of $\boldsymbol{\mathcal{C}}$, we also see that $\mathrm{E}\{\dot{x}_i\, x_j\} = 0$. We, thus, easily conclude that $\mathrm{E}\{\dot{\mathbf{y}}\} = \mathbf{0}$, which equates the autocovariance of $\dot{\mathbf{y}}$ with its autocorrelation.

According to [12], both $\mathbf{x}$ and $\dot{\mathbf{x}}$ follow a Gaussian distribution, which again allows us to apply the results of [18] in developing expressions for the autocovariance matrix of $\dot{\mathbf{y}}$. This leads to

$$\begin{aligned}
\mathrm{E}\{\dot{y}_1\, \dot{y}_1\} &= \beta_1^2\, k_\mathrm{B}\, T\, \left[\mathbf{M}^{-1}\right]_{11} \\
&\quad + \frac{\beta_1\, \beta_3^2\, \beta_1}{Y_3^2}\, (k_\mathrm{B}\, T)^2\, \left(\left[\mathbf{K}^{-1}\right]_{33}\, \left[\mathbf{M}^{-1}\right]_{11}\right. \\
&\quad \left. +2\, \left[\mathbf{K}^{-1}\right]_{13}\, \left[\mathbf{M}^{-1}\right]_{13} + \left[\mathbf{K}^{-1}\right]_{11}\, \left[\mathbf{M}^{-1}\right]_{33}\right) \\
\mathrm{E}\{\dot{y}_1\, \dot{y}_2\} &= \beta_1\, \beta_2\, k_\mathrm{B}\, T\, \left[\mathbf{M}^{-1}\right]_{12} \\
&\quad + \frac{\beta_1\, \beta_3^2\, \beta_2}{Y_3^2}\, (k_\mathrm{B}\, T)^2\, \left(\left[\mathbf{K}^{-1}\right]_{33}\, \left[\mathbf{M}^{-1}\right]_{12}\right. \\
&\quad + \left[\mathbf{K}^{-1}\right]_{23}\, \left[\mathbf{M}^{-1}\right]_{13} + \left[\mathbf{K}^{-1}\right]_{13}\, \left[\mathbf{M}^{-1}\right]_{23} \\
&\quad \left. + \left[\mathbf{K}^{-1}\right]_{12}\, \left[\mathbf{M}^{-1}\right]_{33}\right) \\
\mathrm{E}\{\dot{y}_1\, \dot{y}_3\} &= \beta_1\, \beta_3\, k_\mathrm{B}\, T\, \left[\mathbf{M}^{-1}\right]_{13} \\
\mathrm{E}\{\dot{y}_2\, \dot{y}_2\} &= \beta_2^2\, k_\mathrm{B}\, T\, \left[\mathbf{M}^{-1}\right]_{22} \\
&\quad + \frac{\beta_2\, \beta_3^2\, \beta_2}{Y_3^2}\, (k_\mathrm{B}\, T)^2\, \left(\left[\mathbf{K}^{-1}\right]_{33}\, \left[\mathbf{M}^{-1}\right]_{22}\right. \\
&\quad \left. +2\, \left[\mathbf{K}^{-1}\right]_{23}\, \left[\mathbf{M}^{-1}\right]_{23} + \left[\mathbf{K}^{-1}\right]_{22}\, \left[\mathbf{M}^{-1}\right]_{33}\right)
\end{aligned}$$

TABLE I
PRESCRIBED RANGE OF COEFFICIENTS

β_1	$[1, 10]$
β_2	$[1, 10]$
β_3	$[1, 10]$
X_3	$[5, 20]$

$$\begin{aligned}
\mathrm{E}\{\dot{y}_2\, \dot{y}_3\} &= \beta_2\, \beta_3\, k_\mathrm{B}\, T\, \left[\mathbf{M}^{-1}\right]_{23} \\
\mathrm{E}\{\dot{y}_3\, \dot{y}_3\} &= \beta_3^2\, k_\mathrm{B}\, T\, \left[\mathbf{M}^{-1}\right]_{33}\,.
\end{aligned} \tag{13}$$

While (11) was quadratic, the situation is now simpler, since (13) is a linear system of equations, where the entries $\left[\mathbf{M}^{-1}\right]_{ij}$ of the inverse of the mass matrix are the unknowns, provided the stiffness matrix $\mathbf{K}$ has already been computed according to Section IV-B. For the sake of brevity, we omit here the trivial step of expressing $\mathbf{M}^{-1}$ in terms of $\mathrm{E}\{\dot{y}_i\, \dot{y}_j\}$.

V. EXPERIMENTS

A. Synthetic Validation

We have performed numeric simulations of our system to validate the calculations of this paper. For one typical experiment, we have generated one set of random matrices $\{\mathbf{M}_0, \boldsymbol{\Gamma}_0, \mathbf{K}_0\}$, as explained in Appendix C. We have also generated a large set of N random samples $\mathbf{n}$ that are normally distributed in $\mathcal{N}(0, 1)$ and provide a realization of a white-noise process with flat power spectrum. We have then applied the solution (6) of the Langevin process to filter $\mathbf{n}$ and to obtain N coordinates $\mathbf{x}$, at a random but fixed temperature T_0. We have proceeded in the discrete Fourier domain. The details can be found in Appendix D.

The numerical availability of $\mathbf{x}$ has allowed us to check the similarity between $\mathbf{K}_0$ and $\mathbf{K}_1 = k_\mathrm{B}\, T_0\, \mathbf{C}^{-1}$, even though $\mathbf{x}$ would not be directly accessible in reality. Then, we have drawn one random set of coefficients $\{\beta_1, \beta_2, \beta_3, X_3\}$ from the uniform distributions specified in Table I, and finally, taken the QPD into account by using (8) to transform $\mathbf{x}$ into a sequence of virtual measurements $\mathbf{y}$.

1) Offline Stiffness: The offline determination of the stiffness matrix is usually done using as data the whole sequence $\mathbf{y}$. We have simulated it by producing the QPD-uncorrected sequence $\tilde{\mathbf{x}} = (y_1/\beta_1, y_2/\beta_2, y_3/\beta_3)$, along with $\tilde{\mathbf{K}} = k_\mathrm{B}\, T_0\, \tilde{\boldsymbol{\Sigma}}^{-1}$, where $\tilde{\boldsymbol{\Sigma}}$ is the autocovariance of $\tilde{\mathbf{x}}$. To give this method a chance in the sequel, we have kept the off-diagonal terms of $\tilde{\boldsymbol{\Sigma}}$ and $\tilde{\boldsymbol{\Sigma}}^{-1}$, but we must note that this already goes one step beyond what is commonly done in practice.

2) Online Stiffness: The contribution of this paper is the computation of the stiffness matrix $\mathbf{K}$ according to (12). To obtain it, we have mainly followed the schematics of Fig. 2, except that for algorithmic commodity, we have implemented h as a moving-average filter of length L. We have applied h twice: a first time to get $\bar{\mathbf{y}}$, and a second time to get $\mathbf{S}$. The resulting estimates s_{ij} of the product $((y_i - \bar{y}_i)\, (y_j - \bar{y}_j))$ have then been downsampled by a factor M. Finally, we have produced a single $\mathbf{S}_0$ as the time-average of the downsampled sequence, and determined $\mathbf{K}$ as stated in (12).

Authorized licensed use limited to: EPFL LAUSANNE. Downloaded on June 10,2010 at 13:35:30 UTC from IEEE Xplore. Restrictions apply.

TABLE II
SIMULATION RESULTS FOR THE FULL STIFFNESS MATRIX, BASED ON CROSS CORRELATIONS (SMALLER IS BETTER)

	min	max	median	average
$F(\mathbf{K}_1)$	0.025	0.15	0.061	0.065 ± 0.026
$F(\tilde{\mathbf{K}})$	0.018	1.18	0.102	0.195 ± 0.222
$F(\mathbf{K})$	0.026	0.79	0.075	0.107 ± 0.121

TABLE III
SIMULATION RESULTS FOR TWO ELEMENTS OF THE STIFFNESS MATRIX, BASED ON AVERAGING (SMALLER IS BETTER)

	min	max	median	average
G_{13}	0.0062	1960.5	0.29	20.5 ± 195.9
G_{23}	0.0095	18.6	0.27	0.8 ± 2.2

3) Figure of Merit: We need a figure of merit to compare the virtual measurements $\mathbf{K}_1$, $\tilde{\mathbf{K}}$, and $\mathbf{K}$ to the ground-truth $\mathbf{K}_0$. In this role, we have retained the Frobenius norm $F(\mathbf{Q}) = \left\|\mathbf{Q}\,\mathbf{K}_0^{-1} - \mathbf{I}\right\|$.

We report in Table II the outcome of performing one hundred times the operations of Sections V-A1 and V-A2 with $N = 10^5$ and $L = M = 10^3$. In this case, the two components of the online system that we have simulated would share the computational load in such a way that the analog hardware described in Section IV-A would take care of most "computations," while the load of the digital computer would be $M = 1000$ times less important to get $\mathbf{K}$ than to get $\tilde{\mathbf{K}}$. (Remember that the oracle solution $\mathbf{K}_1$ is not accessible outside of simulations.) Despite that it is computationally more frugal, the average figure of merit of our proposed method is nearly twice better than that of the offline approach. Had we not kept the off-diagonal terms of $\tilde{\mathbf{\Sigma}}$, the comparison would be even more in our favor.

Alternatively, we could have chosen to follow the strategy suggested in (9) to access two out of the six independent components of the stiffness matrix. To focus on these two cases, we propose the following figures of merit: $G_{13} = \left|(\beta_1/X_3)\,k_\mathrm{B}\,T\,\left[\mathbf{K}_0^{-1}\right]_{13}/\bar{y}_1 - 1\right|$ and $G_{23} = \left|(\beta_2/X_3)\,k_\mathrm{B}\,T\,\left[\mathbf{K}_0^{-1}\right]_{23}/\bar{y}_2 - 1\right|$. We present the results in Table III, where we see that (9) lacks in stability when compared to (12), which is therefore the approach that we recommend to get every element of $\mathbf{K}$.

4) Bias: We want now to examine the capacity of our proposed method to cancel the bias that results from the artificial correlations introduced by the QPD detector. As evidenced by inspection of (8) or (12), this bias is most prevalent for small $X_3 \propto Y_3$. Therefore, we suggest to sort the figure of merit according to X_3. As expected, we see in Fig. 4 that the oracle solution $\mathbf{K}_1$ does not depend on X_3. Meanwhile, the offline estimation, which does not attempt to cancel the bias, exhibits a particularly strong error $F(\tilde{\mathbf{K}})$ when X_3 is small—this corresponds to weak trapping (see Fig. 5). Finally, we see in Fig. 6 that our proposed method is able to considerably attenuate the dependence of the error on the depth of modulation. Moreover, the figure of merit comes close to that achieved by the oracle estimator, despite the perturbations introduced by the QPD.

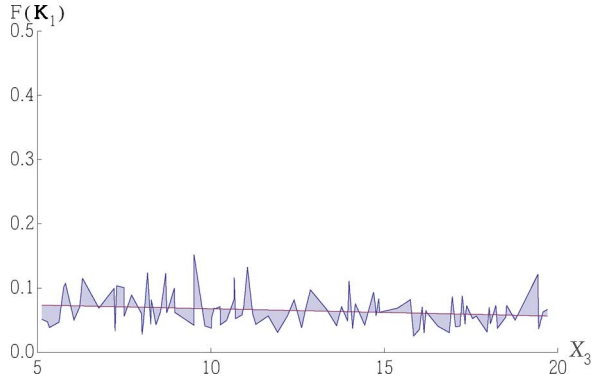

Fig. 4. Repartition of the Monte Carlo error $F(\mathbf{K}_1)$ committed by the oracle estimator in terms of the relative depth of modulation of the laser light, along with the associated linear regression.

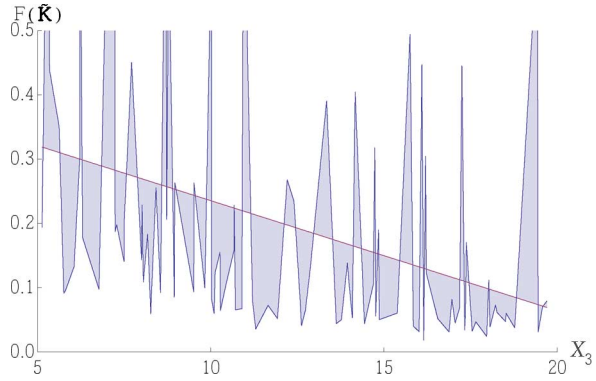

Fig. 5. Repartition of the Monte Carlo error $F(\tilde{\mathbf{K}})$ committed by the offline estimator in terms of the relative depth of modulation of the laser light, along with the associated linear regression.

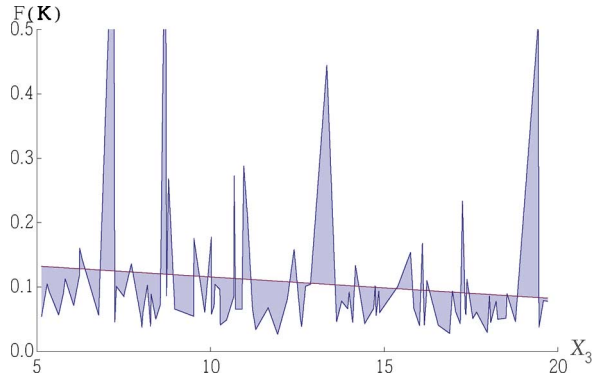

Fig. 6. Repartition of the Monte Carlo error $F(\mathbf{K})$ committed by the proposed estimator in terms of the relative depth of modulation of the laser light, along with the associated linear regression.

B. Real Data

In addition to the synthetic experiments of Section V-A, we have designed and built a real system that couples a PFM to the device proposed in Section IV. To this system, we have added a piezoelectric actuator to move the bead in relation to its surroundings. These large-scale displacements allow us to explore the medium around the bead and are driven by a 3-D joystick that has six degrees of liberty. Then, we have capitalized

Authorized licensed use limited to: EPFL LAUSANNE. Downloaded on June 10,2010 at 13:35:30 UTC from IEEE Xplore. Restrictions apply.

TABLE IV
TIME BETWEEN SAMPLES OF $\mathbf{S}$

$\Delta\tau$ in 10^{-3} s	Occurrences in %
0.1572 ± 0.0089	99.46
0.3087 ± 0.0567	00.11
0.4961 ± 0.0472	00.13
2.6451 ± 0.8735	00.30

TABLE V
SURROGATE GROUND TRUTHS FOR $\tau_0 = 0\,\mathrm{s}$ AND $\Delta t_0 = 11\,\mathrm{s}$

$$\tilde{\mathbf{K}}(\tau_0;\Delta t_0) = \begin{pmatrix} 25.43 & -2.06 & 2.71 \\ -2.06 & 22.44 & -1.08 \\ 2.71 & -1.08 & 4.18 \end{pmatrix} \times 10^{-6}\,\mathrm{N\,m^{-1}}$$

$$\mathbf{K}(\tau_0;\Delta t_0) = \begin{pmatrix} 29.18 & -2.29 & 5.81 \\ -2.29 & 25.76 & -1.06 \\ 5.81 & -1.06 & 17.04 \end{pmatrix} \times 10^{-6}\,\mathrm{N\,m^{-1}}$$

on the fact that we can attain real-time performance to close the measurement loop and to exert feedback forces on the joystick, which therefore acts as a full haptic device. A photograph of the system is available from [9], along with some practical experiments.

In this paper, we want to focus on the real-time capabilities of our system. We have thus synchronously acquired $\mathbf{y}$ and $\mathbf{S}$ over a duration $\Delta t = 11\,\mathrm{s}$, with a sampling frequency of 10^6 and $6.4 \times 10^3\,\mathrm{Hz}$, respectively. The material of the probing bead was polystyrene and its diameter was $10^{-6}\,\mathrm{m}$. It was trapped in pure water at room temperature, taken to be 300 K. The conditions were assumed to remain stable during the duration of the experiment. From these collected data, along with the calibration procedure [17], we could determine that $\beta_1 = 123.5 \times 10^6\,\mathrm{V\,m^{-1}}$, $\beta_2 = 118.9 \times 10^6\,\mathrm{V\,m^{-1}}$, and $\beta_3 = 39.54 \times 10^6\,\mathrm{V\,m^{-1}}$. We also measured $Y_3 = 7.46\,\mathrm{V}$.

1) Jitter: The acquisition of $\mathbf{y}$ is performed by a dedicated system that ensures the stability of the sampling rate. Meanwhile, $\mathbf{S}$ is sampled by a PC that occasionally honors a variety of concurrent real-time tasks. For monitoring purposes, we have recorded a time stamp τ with every sample of $\mathbf{S}$. A breakdown of these time stamps reveals that we rarely miss a beat. However, a wide gap in the data sometimes develops. The details can be seen in Table IV.

2) Surrogate Ground-Truths: To obtain surrogate ground-truths, we estimate $\tilde{\mathbf{K}}(\tau_0;\Delta t_0)$ over the whole available signal, from $\tau_0 = 0\,\mathrm{s}$ and for a duration $\Delta t_0 = 11\,\mathrm{s}$. In parallel, we estimate $\mathbf{K}(\tau_0;\Delta t_0)$ by applying (12) to $\mathbf{S}(\tau_0;\Delta t_0)$ averaged over the whole signal. We provide in Table V the corresponding estimates of stiffness. We observe that the two approaches result in different (but similar) outcomes. At this stage, it is difficult to know which one is closest to the true $\mathbf{K}_0$. Therefore, we are going to keep both versions in the next experiment.

3) Stability: In this section, we check the ability of our system to determine $\mathbf{K}$ on the basis of few data only. We have cut the data in hundred overlapping pieces that last $\Delta t_1 = 1\,\mathrm{s}$ each and that are separated by a tenth of a second. Using the figure of merit of Section V-A3 with the matching surrogate $\mathbf{K}_0$ from Section V-B2, we have built Fig. 7 to show $F(\tilde{\mathbf{K}}(\tau;\Delta t_1))$ and $F(\mathbf{K}(\tau;\Delta t_1))$ in terms of τ. Clearly, the error committed by our proposed combination of hardware and software is

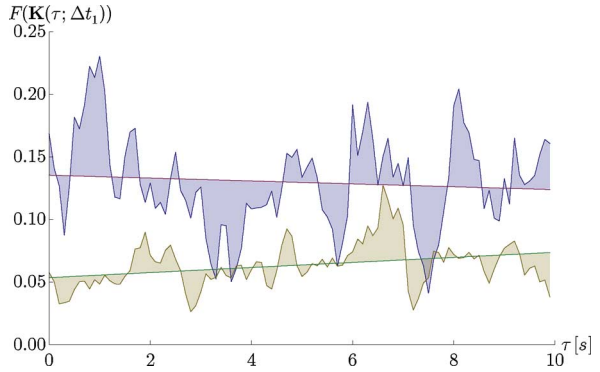

Fig. 7. Error over time of the estimation of stiffness with real data. (Upper trace) Offline approach $\tilde{\mathbf{K}}$. (Lower trace) Our proposed $\mathbf{K}$. In each case, a linear regression is provided.

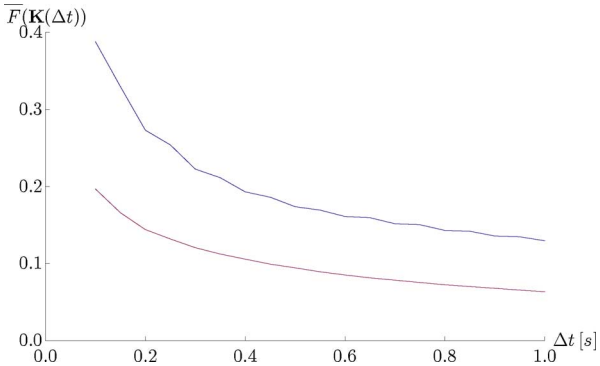

Fig. 8. Average error of the estimation of stiffness with real data in terms of the amount of data used to perform the estimation. (Upper curve) Offline approach $\tilde{\mathbf{K}}$. (Lower curve) Our proposed $\mathbf{K}$.

lower than that of the offline approach. On average, we reach $\bar{F}(\mathbf{K}(\Delta t_1)) = 0.06 \pm 0.02$, which is about twice better than $\bar{F}(\tilde{\mathbf{K}}(\Delta t_1)) = 0.13 \pm 0.04$.

In the next series of experiments, we have observed how $\bar{F}$ evolves when we gradually reduce Δt from 1 to 0.1 s. In Fig. 8, we present the degree of consistency between $\mathbf{K}(\Delta t_0)$ with $\Delta t_0 = 10\,\mathrm{s}$, and $\mathbf{K}(\Delta t)$ with $\Delta t \ll \Delta t_0$. We observe that this consistency remains about twice better for our proposed system than in the case of the offline approach, which certainly suggests that $\mathbf{K}(\tau_0;\Delta t_0)$ is a better estimation of $\mathbf{K}_0$ than $\tilde{\mathbf{K}}(\tau_0;\Delta t_0)$.

VI. CONCLUSION

We have proposed to complement a PFM with a combination of software and low-cost hardware that work hand-in-hand. Their design has been dictated by the Langevin stochastic differential equation that describes the dynamics of the probing bead of the PFM. Our system allows for the real-time estimation of the full symmetric 3-D stiffness matrix found in the Langevin model.

Our analysis reveals that every term associated with the lateral displacements of the probing bead of the PFM is corrupted by a bias. This bias is due to artificial correlations created by a QPD used as the main detector of the PFM. Therefore, we have written our software to fully cancel the QPD-related correlations.

Authorized licensed use limited to: EPFL LAUSANNE. Downloaded on June 10,2010 at 13:35:30 UTC from IEEE Xplore. Restrictions apply.

This cancelation is particularly important because we want to estimate not only the diagonal terms of the stiffness matrix of the PFM, but also its off-diagonal terms. We showed with Monte Carlo simulations that our proposed algorithm results in better accuracy than can be reached in the absence of cancelation.

Our proposed additional hardware involves off-the-shelf electronics; its purpose is to act as an analog computer to preprocess the data. Once preprocessed, the sampling rate can be drastically reduced, which offers us the opportunity to use a standard PC to compute in real-time quantities that otherwise would have required either an offline analysis, or high-performance equipment. We have built this system and shown that it is not only faster but also more accurate than the offline approach to acquire a stiffness matrix. Finally, we have suggested an extension whereby one could similarly access the mass matrix of the probing bead.

APPENDIX A
FILTER UNBIASEDNESS

Let h be the impulse response of a filter that satisfies $\int_{-\infty}^{\infty} h(\tau)\,\mathrm{d}\tau = 1$. We show here that the time average of a weakly stationary signal $\mathbf{x}$ is equal to that of the filtered signal $(h * \mathbf{x})$, since

$$\begin{aligned}\overline{h * \mathbf{x}} &= \overline{\int_{-\infty}^{\infty} h(\tau)\,\mathbf{x}(\cdot - \tau)\,\mathrm{d}\tau} \\ &= \int_{-\infty}^{\infty} h(\tau)\,\overline{\mathbf{x}(\cdot - \tau)}\,\mathrm{d}\tau \\ &= \overline{\mathbf{x}} \int_{-\infty}^{\infty} h(\tau)\,\mathrm{d}\tau \\ &= \overline{\mathbf{x}}.\end{aligned}$$

The same reasoning can be applied to show that the estimated covariance matrix defined in Appendix B is unbiased, too.

APPENDIX B
SEMIPOSITIVE-DEFINITE AUTOCORRELATION

Let h be the real and nonnegative impulse response of an absolutely integrable filter, and let $\mathbf{x}$ be a signal with time average $\bar{\mathbf{x}}$. Moreover, let $\mathbf{C}$ be the estimate of the covariance matrix of $\mathbf{x}$ given by

$$\mathbf{C}(t) = \int_{-\infty}^{\infty} h(\tau)\ (\mathbf{x}(t-\tau) - \bar{\mathbf{x}})\ (\mathbf{x}(t-\tau) - \bar{\mathbf{x}})^{\mathsf{T}}\ \mathrm{d}\tau.$$

Then, $\mathbf{C}$ is semipositive definite because for any signal $\mathbf{x}$, for any vector $\mathbf{u} \neq \mathbf{0}$, and at any time t, we have that

$$\begin{aligned}\mathbf{u}^{\mathsf{T}}\,\mathbf{C}(t)\,\mathbf{u} &= \int_{-\infty}^{\infty} h(\tau)\ \left((\mathbf{x}(t-\tau) - \bar{\mathbf{x}})^{\mathsf{T}}\ \mathbf{u}\right)^2\ \mathrm{d}\tau \\ &\geq 0.\end{aligned}$$

A nonnegative h is not only a sufficient condition, it is also a necessary one. Indeed, consider the particular signal $\mathbf{x}_0(t) = \min(0, h(-t))\,\mathbf{1}$, which has a support Ω_0 that is identical to the support of $h < 0$. Because $h \in L_1$, we have that $\bar{\mathbf{x}}_0 = \mathbf{0}$. Then, under the *a contrario* hypothesis $\Omega_0 \neq \emptyset$, we write

$$\begin{aligned}\mathbf{u}^{\mathsf{T}}\,\mathbf{C}_0(0)\,\mathbf{u} &= \int_{-\infty}^{\infty} h(\tau)\ (\min(0, h(\tau)))^2\ \left(\mathbf{1}^{\mathsf{T}}\,\mathbf{u}\right)^2\ \mathrm{d}\tau \\ &= \left(\sum u_i\right)^2 \int_{\Omega_0} h^3(\tau)\,\mathrm{d}\tau \\ &\leq 0\end{aligned}$$

so that $\mathbf{C}$ is semipositive definite, if and only if $\Omega_0 = \emptyset$.

TABLE VI
PRESCRIBED RANGE OF EIGENVALUES

	λ_1	λ_2	λ_3
$\mathbf{M}_0$	$[1, 5]$	$[1, 5]$	$[1, 5]$
$\mathbf{\Gamma}_0$	$[10, 50]$	$[10, 50]$	$[10, 50]$
$\mathbf{K}_0$	$[1, 5]$	$[1, 5]$	$[0.1, 1]$
T_0	$[1, 10]$		

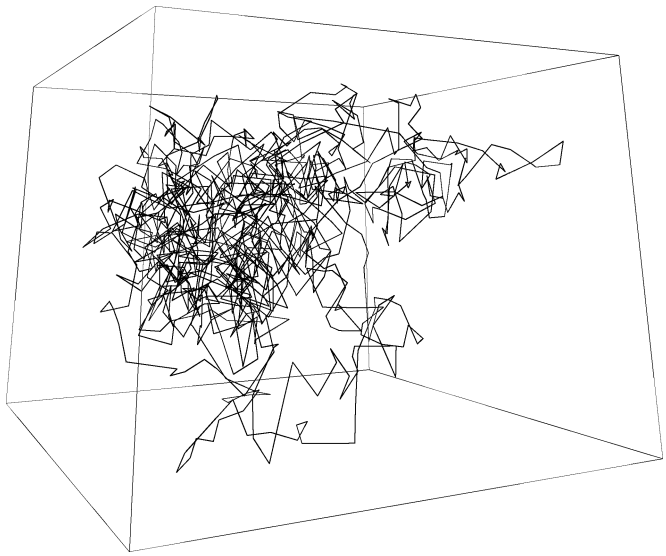

Fig. 9. Path taken by a virtual bead satisfying an idealized Langevin process. In this specific case, the arbitrary random parameters are $\mathbf{M}_0 = \{\{3.39, -0.64, -0.20\}, \{-0.64, 2.96, 0.60\}, \{-0.20, 0.60, 2.19\}\}$, $\mathbf{\Gamma}_0 = \{\{34.65, -6.71, 0.0047\}, \{-6.71, 26.57, -1.40\}, \{0.0047, -1.40, 25.14\}\}$, and $\mathbf{K}_0 = \{\{1.50, 0.35, 1.16\}, \{0.35, 1.18, 1.26\}, \{1.16, 1.26, 2.97\}\}$, with $T_0 = 8.4$.

APPENDIX C
SYNTHESIS OF RANDOM MATRICES

To generate any one of $\{\mathbf{M}_0, \mathbf{\Gamma}_0, \mathbf{K}_0\}$, we have started in each case with a purely random (3×3) matrix $\mathbf{A}_0$, whose entries a_{ij} are uniformly distributed in the range $[-1, 1]$. We have then made it symmetric by computing $\mathbf{A}_1 = \mathbf{A}_0\,\mathbf{A}_0^{\mathsf{T}}$ and expressed it as $\mathbf{A}_1 = \mathbf{V}^{\mathsf{T}}\,\mathbf{\Lambda}_1\,\mathbf{V}$, where $\mathbf{\Lambda}_1$ contains the eigenvalues of $\mathbf{A}_1$ and $\mathbf{V}$ its eigenvectors. Finally, we have substituted the eigenvalues by sorted random numbers uniformly distributed in a prescribed range and built the final matrix as $\mathbf{A} = \mathbf{V}^{\mathsf{T}}\,\mathbf{\Lambda}\,\mathbf{V}$. The force matrix that drives the Langevin process has then been set to $\mathbf{F}_0 = \mathbf{V}_\Gamma^{\mathsf{T}}\,\sqrt{2\,k_{\mathrm{B}}\,T_0\,\mathbf{\Lambda}_\Gamma}\,\mathbf{V}_\Gamma$, where $\mathbf{V}_\Gamma$ and $\mathbf{\Lambda}_\Gamma$ represent the eigendecomposition of $\mathbf{\Gamma}_0$, and where the square root has to be understood componentwise. The temperature T_0 also follows

Authorized licensed use limited to: EPFL LAUSANNE. Downloaded on June 10,2010 at 13:35:30 UTC from IEEE Xplore. Restrictions apply.

a prescribed uniform distribution. In the simulation world, we have set $k_{\mathrm{B}} = 1$.

We give in Table VI the range of eigenvalues, which we have chosen arbitrarily. We have enforced that the third eigenvalue of $\mathbf{K}_0$ differs markedly from the two others, which simulates the difference in axial and lateral trapping of the bead. However, the corresponding eigenvector is left free to align (or not) with the third axis of the system of coordinates.

APPENDIX D

SYNTHESIS OF THE LANGEVIN PROCESS

We have generated N positions of the bead by filtering the sequence $(\mathbf{F}_0\ \mathbf{n})$ by ρ, as explained for the 1-D case in Section II-B. More precisely, we have proceeded in Fourier and computed $\check{\mathbf{x}}[n] = \left(-\nu_n^2\,\mathbf{M}_0 + \mathrm{j}\,\nu_n\,\mathbf{\Gamma}_0 + \mathbf{K}_0\right\}\right)^{-1}\,\mathbf{F}_0\,\check{\mathbf{n}}(\nu_n)$, with $\nu_n = (2\,\pi/N)\ (((n + \lceil N/2 \rceil - 1) \bmod N) - \lceil N/2 \rceil + 1)$, where $\check{\mathbf{n}}$ is the discrete Fourier transform of the sequence $\mathbf{n}$, computed as $\forall n \in [0 \ldots N-1] : \check{\mathbf{n}}[n] = \sum_{k=0}^{N-1}\ \mathbf{n}[k]\,\mathrm{e}^{-\mathrm{j}\,2\,\pi\,(n\,k)/N}$. An inverse discrete Fourier transform has then been applied to obtain $\forall k \in [0 \ldots N-1] : \mathbf{x}[k] = (1/N)\sum_{n=0}^{N-1}\ \check{\mathbf{x}}[n]\,\mathrm{e}^{\mathrm{j}\,2\,\pi\,(k\,n)/N}$. We illustrate this construction in Fig. 9, where we show a short sequence of $N = 10^3$ coordinates joined by straight lines.

ACKNOWLEDGMENT

The authors would like to thank Prof. G. Dietler for his friendly support.

REFERENCES

[1] A. Pralle, E.-L. Florin, E. Stelzer, and J. Hörber, "Local viscosity probed by photonic force microscopy," *Appl. Phys. A (Mater. Sci. Process.)*, vol. 66, pp. S71–S73, Mar. 1998.

[2] S. Yamada, D. Wirtz, and S. Kuo, "Mechanics of living cells measured by laser tracking microrheology," *Biophys. J.*, vol. 78, no. 4, pp. 1736–1747, Apr. 2000.

[3] Y. Tseng, T. Kole, and D. Wirtz, "Micromechanical mapping of live cells by multiple-particle-tracking microrheology," *Biophys. J.*, vol. 83, no. 6, pp. 3162–3176, Dec. 2002.

[4] C. Tischer, A. Pralle, and E.-L. Florin, "Determination and correction of position detection nonlinearity in single particle tacking and three-dimensional scanning probe microscopy," *Microsc. Microanal.*, vol. 10, no. 4, pp. 425–434, Aug. 2004.

[5] I. Tolić-Nørrelykke, E.-L. Munteanu, G. Thon, L. Oddershede, and K. Berg-Srensen, "Anomalous diffusion in living yeast cells,," *Phys. Rev. Lett.*, vol. 93, no. 7, pp. 078 102–1–078 102–4, Aug. 13, 2004.

[6] C. Guzmán, H. Flyvbjerg, R. Köszali, C. Ecoffet, L. Forró, and S. Jeney, "*In situ* viscometry by optical trapping interferometry," *Appl. Phys. Lett.*, vol. 93, no. 18, pp. 184102-1–184102-3, Nov. 3, 2008.

[7] S. Jeney, E. Stelzer, H. Grubmüller, and E.-L. Florin, "Mechanical properties of single motor molecules studied by three-dimensional thermal force probing in optical tweezers," *ChemPhysChem*, vol. 5, no. 8, pp. 1150–1158, Aug. 2004.

[8] C. Tischer, S. Altmann, S. Fišinger, J. Heinrich Hörber, E. Stelzer, and E.-L. Florin, "Three-dimensional thermal noise imaging," *Appl. Phys. Lett.*, vol. 79, no. 23, pp. 3878–3880, Dec. 2001.

[9] E. Bertseva, A. Singh, J. Lekki, P. Thévenaz, M. Lekka, S. Jeney, G. Gremaud, S. Puttini, W. Nowak, G. Dietler, L. Forró, M. Unser, and A. Kulik, "Intracellular nanomanipulation by a photonic-force microscope with real-time acquisition of a 3-D stiffness matrix," *Nanotechnology*, vol. 20, no. 28, pp. 285709-1–285709-9, Jul. 15, 2009.

[10] S. Jeney, B. Lukić, J. Kraus, T. Franosch, and L. Forró, "Anisotropic memory effects in confined colloidal diffusion," *Phys. Rev. Lett.*, vol. 100, no. 24, pp. 240604-1–240604-4, Jun. 20, 2008.

[11] A. Rohrbach, C. Tischer, D. Neumayer, E.-L. Florin, and E. Stelzer, "Trapping and tracking a local probe with a photonic force microscope," *Rev. Sci. Instrum.*, vol. 75, no. 6, pp. 2197–2210, Jun. 2004.

[12] M. Wang and G. Uhlenbeck, "On the theory of the Brownian motion II," *Rev. Modern Phys.*, vol. 17, no. 2–3, pp. 323–342, Apr./Jul. 1945.

[13] I. Horenko, C. Hartmann, and C. Schütte, "Data-based parameter estimation of generalized multidimensional Langevin processes," *Phys. Rev. E*, vol. 76, no. 1, pp. 016706-1–016706-9, Jul. 2007.

[14] M. Unser and T. Blu, "Generalized smoothing splines and the optimal discretization of the Wiener filter," *IEEE Trans. Signal Process.*, vol. 53, no. 6, pp. 2146–2159, Jun. 2005.

[15] M. Unser and T. Blu, "Cardinal exponential splines. Part I—Theory and filtering algorithms," *IEEE Trans. Signal Process.*, vol. 53, no. 4, pp. 1425–1438, Apr. 2005.

[16] A. Rohrbach and E. Stelzer, "Three-dimensional position detection of optically trapped dielectric particles," *J. Appl. Phys.*, vol. 91, no. 8, pp. 5474–5488, Apr. 2002.

[17] M. Allersma, F. Gittes, M. deCastro, R. Stewart, and C. Schmidt, "Two-dimensional tracking of ncd motility by back focal plane interferometry," *Biophys. J.*, vol. 74, no. 2, pp. 1074–1085, Feb. 1998.

[18] K. Triantafyllopoulos, "On the central moments of the multidimensional Gaussian distribution," *Math. Sci.*, vol. 28, no. 2, pp. 125–128, Dec. 2003.

Authors' photographs and biographies not available at the time of publication.

Authorized licensed use limited to: EPFL LAUSANNE. Downloaded on June 10,2010 at 13:35:30 UTC from IEEE Xplore. Restrictions apply.